energies

MDPI

Article

The Voltage Control Strategy of a DC-Link Bus Integrated Photovoltaic Charging Module in a Unified Power Quality Conditioner

Fuyin Ni [1,2], Zhengming Li [1,*] and Qi Wang [2]

[1] School of Electrical and Information Engineering, Jiangsu University, Zhengjiang 212013, China; thimbed@163.com

[2] School of Electrical and Information Engineering, Jiangsu University of Technology, Changzhou 213001, China; lzming@ujs.edu.cn

* Correspondence: lzming@ujs.edu.cn; Tel.: +86-13705286653

Received: 3 March 2019; Accepted: 13 May 2019; Published: 15 May 2019

Abstract: In order to improve the functionality and efficiency of a unified power quality conditioner (UPQC), a DC-link bus integrated photovoltaic charging module is proposed in a UPQC. It can generate power for essential loads apart from providing energy to a DC-link bus. A conventional proportional integral (PI) controller fails to run smoothly in dynamic conditions of the micro-grid, since it has poor capabilities in determining suitable values of proportional gain and integral gain. So, the optimization algorithm for a PI controller based on chaos particle swarm optimization based on a multi-agent system (CPSO-MAS) algorithm was developed in this paper to overcome properties such as intermittent instability in the micro-grid. Through verification by simulation and experiment of UPQC harmonic compensation, it showed that the proposed DC link bus voltage control strategy can be effectively applied to UPQC towards various conditions related to voltage and current distortion. In addition, it proved that the proposed strategy has faster convergence than other algorithms, which enhances the stability of DC-link bus voltage. Hence, the contribution presented in this paper is to provide a novel approach for the power quality improvement of UPQC.

Keywords: chaos particle swarm optimization based on multi-agent system algorithm; unified power quality conditioner; micro-grid; power quality; current harmonics

1. Introduction

In recent years, the fast development of renewable energy sources provides a desired solution to the contradiction between energy and environment. The micro-grid appearing in this background is composed of distributed generation, energy storing devices, energy conversion device, loads and protection devices, etc. The micro-grid has characteristics such as like intermittency and volatility. So, the micro-grid connects to the utility grid, and the non-linear current output causes the frequency deviation of the utility grid and voltage fluctuation. With the increased proliferation of renewable energy such as solar and wind, micro-grid power generation brings more serious power quality problems towards the distribution systems [1,2].

Among all kinds of power quality improvement devices, the unified power quality conditioner (UPQC) has become major concern due to the perfect functionality for mitigation of voltage distortion and current perturbations [3–6]. The UPQC is composed of a series active power filters (SAPFs) and paralleled active power filters (PAPFs) [7]. It not only can compensate reactive power and harmonic and negative sequence currents that are caused by non-linear loads or other electrical equipment, but can also compensate the voltage distorted at the source side [8–11]. After a rigorous literature survey was conducted, it can be summarized that the research on UPQCs is mainly focused on its

topology, compensation instruction detection, compensation control strategy, etc. [12–25]. In regard to topology, a novel ten-switch topology for unified power quality conditioner was proposed in Reference [12]. A transformer-less unified power quality conditioner with fast dynamic control was proposed in Reference [14]. As for the power quality analysis, an output regulation-based unified power quality conditioner with Kalman filters was reported in Reference [15]. A UPQC voltage sag detection based on the chaotic immune genetic algorithm was proposed in Reference [16]. As for a control strategy, there is literature focused on control of UPQCs [17–25]. A coordinated control strategy based on reactive power flow in a UPQC was proposed in Reference [19]. Furthermore, the optimal design and control implementation of a UPQC based on variable phase angle control method was proposed in Reference [22]. Improvement of unified power quality conditioner performance with an enhanced resonant control strategy was proposed in Reference [24].

As for the problem of DC voltage control in a UPQC, in Reference [25], a small signal stability model was developed based on the small signal stability and dynamic interaction problems caused by operation mode-switching in a UPQC. The stability and dynamic characteristics between an independent converter operating mode and combined series and parallel converter operating mode were analyzed. It was concluded that the control parameters of the DC bus voltage of the UPQC had a great influence on the small disturbance stability of the UPQC when switching operation mode, and in Reference [26], the causes and the inevitability of the fluctuation of voltage on the DC side of UPQC was also discussed in detail. In Reference [27], a proportional integral (PI) controller was used to maintain the voltage around the reference value for the DC-link side. Theparameters perturbation and load change simulation experiments were performed to verify the effectiveness, robustness, and reliability of the proposed control strategy. In Reference [28], a novel control strategy was presented using a brain emotional learning-based intelligent controller, according to the structure and emotion processing mechanism of a brain emotional learning computational model, and a multi-objective control strategy was proposed for a UPQC device based on the proposed controller. In Reference [29], since the DC-link voltage of the UPQC significantly deviates from its reference during a transient event, caused by load connection/disconnection or/and supply-side voltage sag/swell, an adaptive DC-link voltage controller was proposed which limits the DC link voltage deviation during transients and assures a negligible steady-state error. Therefore, the effectiveness of the proposed control schemes were demonstrated through simulations.

In the above reviewed literature, the PI control strategy was still the key solution for DC-link voltage control. On the condition of voltage sag, the DC-link bus of the UPQC plays a great role in the interchange of the energy of the series active power filter (SAPF) and parallel active power filter (PAPF). The PAPF compensates reactive power for load sides and extracts active power from the power grid to compensate DC-link bus voltage sag because of active power consumption in the SAPF. The energy coupling effect between the two filters decreases the stability of the DC-link bus, thus deteriorating UPQC performance. In addition, photovoltaic (PV) cell generation has the nature of intermittence and instability which can cause the DC-link bus voltage of UPQC to become unstable easily. Therefore, a new control scheme for the DC-link bus integrated with a PV charging module in the UPQC is proposed in this paper. To be specific, an optimization algorithm for a PI controller based on the chaos particle swarm optimization based on a multi-agent system (CPSO-MAS) is developed to overcome the issue of dynamic conditions involved in the micro-grid.

A conventional PI controller fails to perform well in the dynamic conditions of the micro-grid due to its poor ability to determine the appropriate values of proportional gain and integral gain. However, the proposed algorithm can optimize both parameters of the voltage loop PI controller. To further verify the effectiveness of the proposed scheme, a simulation and a scaled down laboratory prototype of the UPQC was developed. Through both simulation and experiment with the UPQC harmonic compensation, the compensated current waveform derived from the CPSO-MAS algorithm was proved fairly smooth and nearly sinusoidal towards various conditions in the micro-grid. Besides,

the total harmonic distortion (THD) value based on the spectrum of the current waveform meets the national standard of power quality.

2. UPQC Mathematical Modeling

The PV micro-grid with the structure of three-phase three-wire presents a topology diagram as shown in Figure 1. The UPQC was installed in the distribution system where the SAPF was placed at the source side and the PAPF was presented at the load side sharing the common DC-link, respectively [30]. The common DC-link was connected by a capacitor. The PV array 1 was connected to the distribution line, and the PV array 2 was integrated to the common DC-link through the boost circuit for charging, and providing energy required for voltage compensation for the SAPF. Moreover, the PV array 2 can be also utilized to the critical load through the PAPF in the event of a power outage. The SAPF utilized to compensate the power supply voltage at the source side is interfaced to the grid through a transformer. The transformer can isolate the inverter from the power grid. The PAPF interfaced with the LC filter was connected to the non-linear load, and it was mainly used for compensation of harmonic current and reactive power.

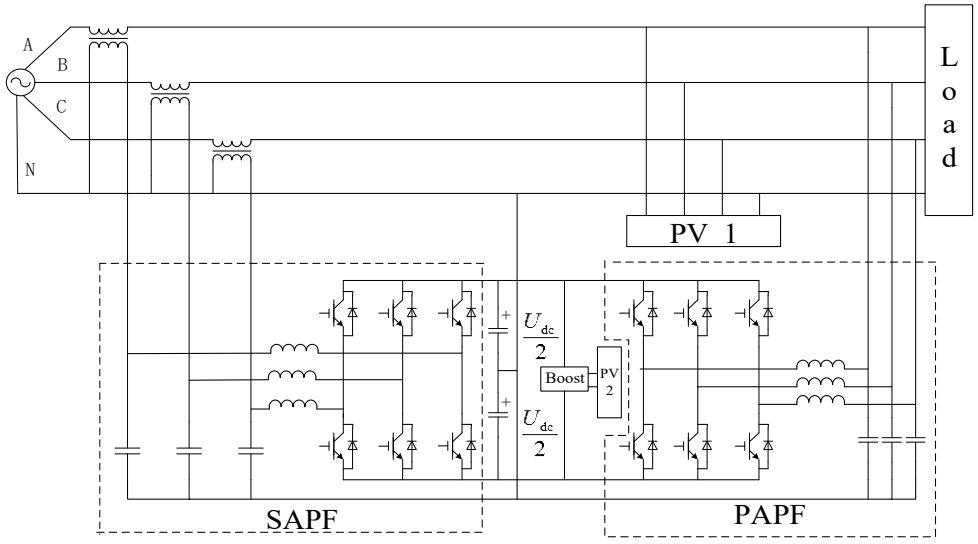

Figure 1. The topology of the UPQC in the PV micro-grid.

The equivalent circuit can be presented with a two-phase static coordinate, and the *d*-axis equivalent circuit is shown in Figure 2.

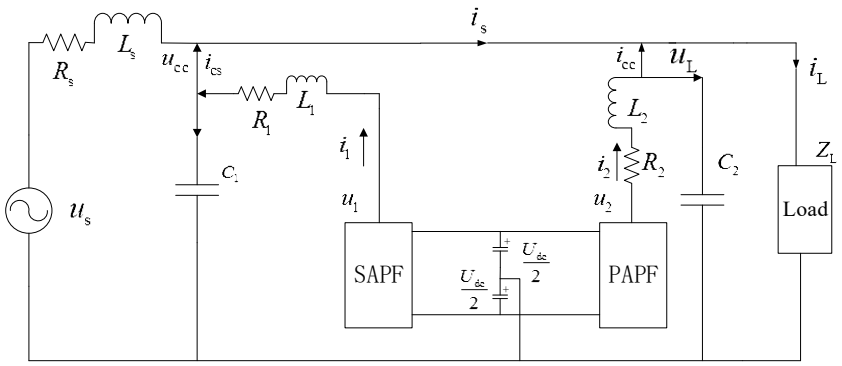

Figure 2. Equivalent circuit based on the *d*-axis.

Where u_s is the grid voltage and i_s is the grid current. i_L the is load current, u_L is the load voltage, u_1 is the output voltage of the SAPF, and u_2 is the output voltage of the PAPF. R_s denotes the sum of the

line resistance and leakage resistance of the series transformer. L_s denotes the sum of the inductance and leakage inductance of the series transformer. L_1 and C_1 are, respectively, the capacitance and inductance of the LC filter in the SAPF. L_2 and C_2 are, respectively, the capacitance and inductance of the LC filter in the PAPF. R_1 and R_2 are, respectively, the equivalent resistance in the SAPF and PAPF. i_1 and i_2 are, respectively, the inductive current in the SAPF and PAPF. i_{cs} and i_{cc} are, respectively, the input current to the distributed line from the SAPF and PAPF. u_{dc} is the voltage of the DC-link bus and C_{dc} is the capacitance interfaced to the DC-link bus.

As for the UPQC, if u_s is stable, the SAPF will bypass, and the PAPF will improve the power factor in the distribution system by injecting reactive power. When u_s drops, the SAPF will output the compensation voltage. u_L is maintained in the normal range to make sensitive loads run stably. Then, the PAPF extracts active power from the grid and keeps the DC-link bus voltage stability. Let the equivalent parallel resistance of the DC-link bus loss be R_{dc}. Suppose that the load is a nonlinear load which includes R_L and L_L.

The PAPF of the UPQC mathematical model is presented in Equation (1) [25]:

$$\begin{cases} L_2 \frac{di_{2d}}{dt} = u_{2d} - R_2 i_{2d} + \omega L_2 i_{2q} - u_{Ld} \\ L_2 \frac{di_{2q}}{dt} = u_{2d} - R_2 i_{2q} - \omega L_2 i_{2d} - u_{Lq} \\ C_2 \frac{du_{Ld}}{dt} = i_{2d} - i_{ccd} + \omega C_2 u_{Lq} \\ C_2 \frac{du_{Lq}}{dt} = i_{2q} - i_{ccq} - \omega C_2 u_{Ld} \end{cases} \quad (1)$$

The SAPF of the UPQC mathematical model is presented as below:

$$\begin{cases} L_1 \frac{di_{1d}}{dt} = u_{1d} - R_1 i_{1d} - u_{ccd} + \omega L_1 i_{1q} \\ L_1 \frac{di_{1q}}{dt} = u_{1q} - R_1 i_{1q} - u_{ccq} - \omega L_1 i_{1d} \\ C_1 \frac{du_{ccd}}{dt} = i_{1d} - i_{csd} + \omega C_1 u_{ccq} \\ C_1 \frac{du_{ccq}}{dt} = i_{1q} - i_{csq} - \omega C_1 u_{ccd} \end{cases}$$

The DC-link bus of UPQC mathematical model is presented in Equation [25] (2):

$$\begin{cases} L_L \frac{di_{Ld}}{dt} = -R_L i_{Ld} + \omega L_L i_{Lq} + u_{Ld} \\ L_L \frac{di_{Lq}}{dt} = -R_L i_{Lq} - \omega L_L i_{Ld} + u_{Lq} \end{cases} \quad (2)$$

As for the PAPF of the UPQC, the UPQC only compensates the harmonic and reactive current which is affected by loads, and the active current $i_p = 0$. The three-phase instantaneous reactive current i_q cannot lead to the exchange energy with the utility grid. Therefore, the UPQC exchanges energy with the grid because of the active current i_p. So, the conventional DC-link bus voltage of the UPQC is controlled by injecting active current i_p from the grid.

The PV charging scheme is provided to keep the DC-link bus stable. Therefore, the DC-link bus can obtain energy from the PV cell. However, the drawback is that it is difficult to control it perfectly due to the dynamic conditions such as volatile temperature. So, it is necessary to exploit a better control strategy to ensure the voltage stability and the UPQC performance.

3. The Control Scheme of the DC-Link Bus Integrated PV Charging Module in UPQC

3.1. DC-Link Bus Integrated PV Charging Scheme

The charging control scheme of the DC-link bus integrated PV cell is shown in Figure 3. The energy of the PV cell is fed into the DC-link bus through a DC/DC converter, which is based on the main micro-controller DSP (Digital signal processor) (TMS320F28335).

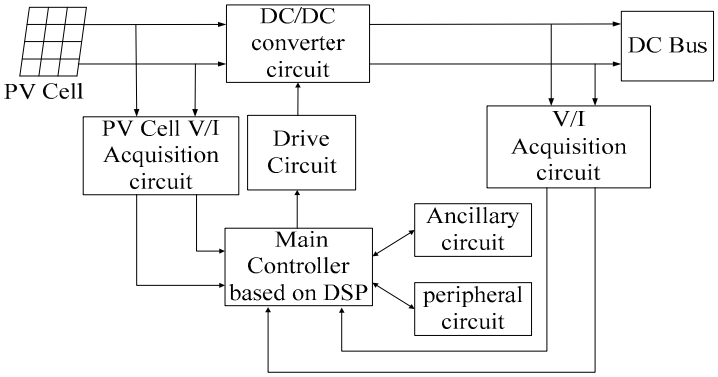

Figure 3. Charging control scheme of the DC-link bus integrated PV cell.

The DC/DC conversion is realized by the boost increment circuit in the PV charging module as shown in Figure 4 [31].

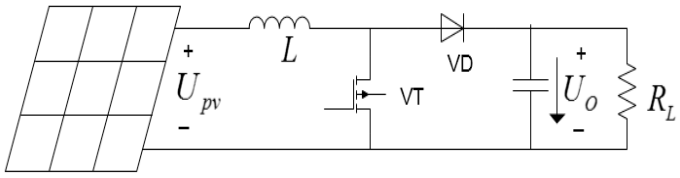

Figure 4. Boost increment circuit in the PV charging module.

Where U_{pv} is the photovoltaic output voltage, R_L is the load, and L is the inductance. The output voltage of the boost circuit is given as [31]:

$$U_{pv} \cdot D \cdot T + (U_{pv} - U_0) \cdot (1 - D \cdot T) = 0 \tag{3}$$

where T is the switching cycle of the tube, D is the duty cycle, and the output voltage U_o of the boost increment circuit is given as:

$$U_0 = \frac{1}{1 - D} U_{pv} \tag{4}$$

The boost conversion equivalent circuit is presented in Figure 5.

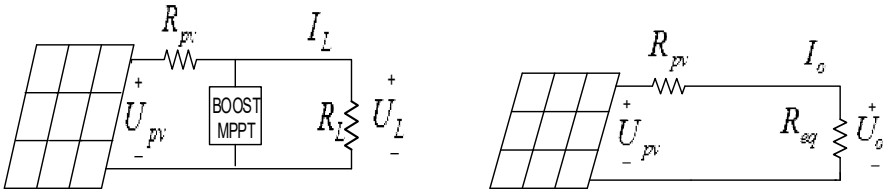

Figure 5. Boost conversion equivalent circuit.

Where R_{pv} is the resistance of the PV array and I_L is the photovoltaic current at the load side. According to the equivalent circuit,

$$U_o = U_L \cdot (1 - D) \tag{5}$$

Since the power is equal in the conversion, the output current I_o of the boost circuit is given as:

$$I_o = I_L / (1 - D) \tag{6}$$

Thereby, the equivalent resistance R_{eq} is calculated as:

$$R_{eq} = \frac{U_o}{I_o} = \frac{U_L \cdot (1-D)}{I_L/(1-D)} = R_L \cdot (1-D)^2 \tag{7}$$

Once R_{eq} is equal to R_{pv} by adjusting the duty cycle D, the injected max power is expressed in Equation (8):

$$P_{\max} = \left(\frac{U_{PV}}{R_{pv} + R_{eq}}\right)^2 \cdot R_{eq} = \frac{{U_{pv}}^2}{4R_{eq}} \tag{8}$$

As the DC-link bus voltage is set to be 600 V, the max power point tracking control strategy adopts a constant voltage control strategy in the PV cell.

3.2. PV Charging Control Strategy

The control strategy is developed by an outer voltage loop and an inner current loop in the DC/AC converter. The proposed double closed-loop control strategy of the photovoltaic generation is shown in Figure 6.

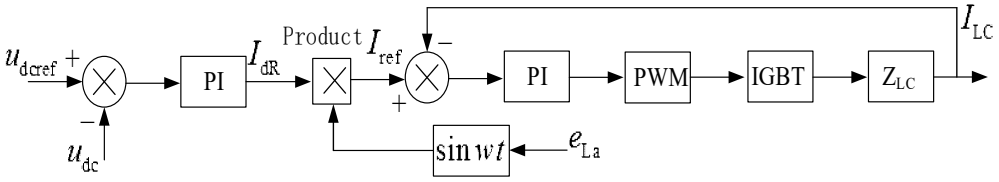

Figure 6. PV charging control strategy diagram.

Where the reference voltage u_{dcref} is set to be 600 V. u_{dc} is the output voltage of the boost converter. The u_{dcref} and u_{dc} form an outer voltage loop and generate current I_{dR}. The current I_{dR} products the sinusoidal signal from the grid voltage e_{La}, the reference current I_{ref} is then obtained. After that, the grid currents I_{LC} and I_{ref} form the inner current loop. The output from the internal PI control is the PWM (Pulse width modulation) signal which control the IGBT. Thereby the control strategy can also be expressed in Figure 7.

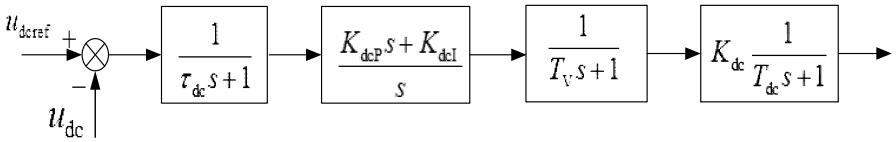

Figure 7. The DC-link bus voltage control diagram of the UPQC.

Where τ_{dc} is the DC-link bus sampling delay time constant, K_{dcP} is the proportional parameter of the DC-link bus PI controller, and K_{dcI} is the integral parameter of the DC-link bus PI controller. The expression of the inner current loop is simplified and represented as:

$$G_V(s) = \frac{1}{T_V s + 1} \tag{9}$$

where T_V is the equivalent time constant.

Then, the transfer function of the DC-link bus voltage open-loop system is presented as [32]:

$$G_{dc}(s) = \frac{K_{pwm}(K_{dcP}s + K_{dcI})}{s(\tau_{dc}s+1)(T_V s+1)\left(T_{pwm}s+1\right)} \tag{10}$$

where set τ_{dc} = 0.0001s, T_V = 0.0005s [32]. $G_{dc}(s)$ is represented simply as:

$$G_{dc}(s) = \frac{K_{pwm}(K_{dcP}s + K_{dcI})}{s(0.6s+1)\left(T_{pwm}s+1\right)} \tag{11}$$

where K_{dc} is set to be 2, $K_{dcP}/K_{dcI} = T_{pwm}$, and $G_{dc}(s)$ is represented as:

$$G_{dc}(s) = \frac{2}{s(0.6s+1)}K_{dcI} \tag{12}$$

4. The Optimization Algorithm for a PI Controller of a DC-Link Bus Integrated PV Charging Module

4.1. Particle Swarm Optimization Algorithm

The particle swarm optimization (PSO) algorithm is an evolutionary computation based on swarm intelligence [28]. The algorithm originates from the simulation of the clustering behavior of birds and fish. In the algorithm, every individual is thought to be a particle whose mass and volume is neglected. The individual has the property of speed and position, and another fitness value that determines the particle performance. Then these particles form a swarm. The particle changes its own action and makes progress to the optimal direction through the sharing of information and its own experience when it is searching.

According to the PSO algorithm, the particles are initialized to be a bunch of random particles firstly. Then they search for the optimal solution by iteration. In every iteration, they obtain the information that includes individual optimum p_{best} and global optimum g_{best} by sharing information. Herein, p_{best} is the optimal solution that the particle searches by itself. g_{best} is the optimal solution that the entire population searches. Then, the particles update their action according to the shared information. Consider a swarm with N particles stored in the D-dimension searching space. The position vector x_i and speed vector v_i of the i^{th} particle are given as [33]:

$$\begin{cases} x_i = (x_{i1}, x_{i2}, \cdots, x_{iD}), i = 1, 2, \cdots, N \\ v_i = (v_{i1}, v_{i2}, \cdots, v_{iD}), i = 1, 2, \cdots, N \end{cases} \tag{13}$$

The i^{th} particle updates the speed and position at the searching space according to Equation (14).

$$\begin{cases} v_{t+1} = w_t v_t + c_1 r_1 (p_{best} - x_t) + c_2 r_2 (g_{best} - x_t) \\ x_{t+1} = x_t + v_{t+1} \end{cases} \tag{14}$$

where t is iteration times and x_t is the particle space position of t^{th} iteration. v_t is the particle speed of the t^{th} iteration. w_t is the inertia constant. c_1, c_2 is the study factor. r_1, r_2 is the random value with the range of (0, 1).

A standard flowchart of the PSO is shown in Figure 8.

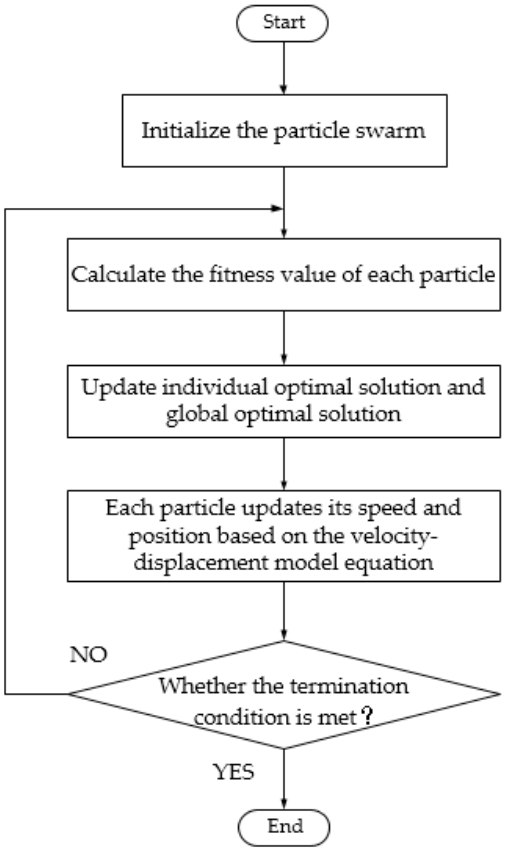

Figure 8. A standard PSO flow chart.

Compared to genetic algorithms, PSO is easier to perform and faster to converge due to the presence of fewer parameters. Thus, a number of PSO-based algorithms have been developed to get better control performance [34–36].

4.2. Particle Swarm Optimization Based on Multi-Agent System Algorithm

Particle swarm optimization based on a multi-agent system algorithm (PSO-MAS) is an improved algorithm characterized by the features of a PSO algorithm and multi-agent system [33,34]. Each particle can be viewed as an agent, so each particle not only updates the evolution principle of the PSO algorithm, but also participates in the competition and cooperation with its neighbor. Then, it exchanges information with global optimal particle and updates the current speed and position of particles in accordance with its own experience and the global optimum. Thereby, the particles change the strategy and improve the convergence speed and optimization ability of the swarm.

It is assumed that any agent in the swarm is α, which is equivalent to a particle in the PSO algorithm. Each particle corresponds to a fitness value determined by the optimization problem. As for the DC-link voltage loop PI controller, the agent fitness function is determined in Equation (15).

$$f(\alpha) = f \tag{15}$$

The agent α employs to corresponding action with the environment and makes the fitness value optimal under the premise of satisfying the constraint conditions.

Every agent is randomly initialized in an environment with a total number of $L_{\text{size}} \times L_{\text{size}}$ grids. Each agent occupies a grid. The data in the grid represents the position information in the environment of agent. Each agent itself contains two data information of the speed and position of each particle in PSO. L_{size} is a positive integer. The total number of cells corresponds to the swarm size in a PSO. In addition, a local environment needs to be defined to obtain the basis for supporting the particle's

next action strategy. In the local environment model, the coordinates (x, y) are used to represent the physical position of the particle. Let $L_{i,j}$ denote the current particle whose coordinates are (x, y), where, $i, j = 1, 2, \cdots, L$, (L represents the global environment), the local environment of $L_{i,j}$ is defined as $N_{i,j}$ [33]:

$$N_{i,j} = \left\{ L_{i_1,j}, L_{i,j_1}, L_{i_2,j}, L_{i,j_2} \right\} \tag{16}$$

$$i_1 = \begin{cases} i_1 = i-1, i \neq 1 \\ L, i = 1 \end{cases} \quad j_1 = \begin{cases} j_1 = j-1, j \neq 1 \\ L, j = 1 \end{cases}$$
$$i_2 = \begin{cases} i = i+1, i \neq L \\ 1, i = L \end{cases} \quad j_2 = \begin{cases} j = j+1, j \neq L \\ 1, j = L \end{cases}$$

In the PSO-MAS algorithm, each agent has to compete and cooperate with $N-1$ particles in the local environment. It is assumed that the current agent is $L_{i,j}$ and $M_{i,j}$ is obtained after competition and cooperation. So, $M_{i,j}$ is the agent whose fitness value is minimum in its neighbor particles. If the fitness value of the current particle is less than the fitness value of the optimal neighbor particle, its performance is better. The position in the solution remains unchanged. Otherwise, search and update will be conducted according to the following equation to the approaching position [34]:

$$\begin{cases} f(L_{i,j}) \leq f(M_{i,j}) \\ L'_{i,j} = M_{i,j} + rand(-1,\ 1)(L_{i,j} - M_{i,j}) \end{cases} \tag{17}$$

In accordance with Equation (17), even if the current agent is replaced, it still retains its original useful information and fully absorbs the useful information of its neighbors. Therefore, the PSO-MAS algorithm not only enhances the evolutionary performance of the multi-agent system, but also increases the population diversity of the particle swarm which makes information update between agents faster and more efficient.

4.3. Chaos Local Search

Chaos is a complex and irregular behavior generated by non-linear systems. But the seemingly irregular chaotic movement has exquisite internal regularity. It has the characteristics of randomness, ergodicity, and sensitivity to initial conditions. The chaos local search (CLS) algorithm begins at a possible solution of a problem and searches for a solution which reaches a certain standard [37]. The solution replaces the original solution and continues to iterate until the total number of iterations reaches the preset upper limit. In the process of calculation, the CLS retains a certain number of fine particles and shrinks the region dynamically according to the swarm's best position. The many neighborhood points of the local optimal solution are produced in the iteration. These random particles replace the particles of poor performance in the shrinking region so that the search process has the ability to avoid falling into local minima.

4.4. The Optimization Algorithm for a PI Controller Based on CPSO-MAS

Due to the good performance of CPSO-MAS, this algorithm can be applied to regulate parameters of voltage PI loop in the photovoltaic charging module, as shown in Figure 6. The DC-link bus reference voltage $u_{\mathrm{dc}ref}$ was set to be 600 V. The calculated error between $u_{\mathrm{dc}ref}$ and u_{dc} is the input to the PI controller. The optimization algorithm steps for CPSO-MAS-based PI controller are as follows:

(1) Initialization and parameter setting. The grid environment based on the multi-agent system is constructed, and each agent is equipped with eight neighboring particles, which constitutes a local environment of interactive communication together. In this multi-agent environment, the particle swarm number was set to 100, maximum allowable iteration number was set to 100, and inertia weight was set to 0.63. The learning factor was set to 1.28. The particle's position and velocity in the solution space was initialized. Parameters K_{dcP} and K_{dcI} were set with the range of (15, 50) and (0.15, 0.86), respectively.

(2) Objective function evaluation. The objective function is given as [33]:

$$J = \int_0^\infty \{[w_1|e(t)| + w_2u^2(t) + w_4|ey(t)|] + w_3t_u\}dt \tag{18}$$

w_1, w_2, w_3, w_4 are weights, and $w_4 >> w_1$, $ey(t) = y(t) - y(t-1)$, $y(t)$ is the output of the controlled voltage u_{dc}. $u(t)$ denotes I_{dR} as shown in Figure 6, i.e., the output of the PI controller. Thereby, a set of PI control parameters (K_{dcP}, K_{dcI}) is obtained to minimize the value of the system objective function J based on CPSO-MAS so that the generated current I_{dR} will perform satisfactorily for UPQC towards various conditions related the distorted voltage and current.

(3) Fitness recalculation after particle agent competition and cooperation. Each particle agent competes and cooperates with eights neighbors and updates the fitness value. According to the action strategy formula [33]:

$$f(a) \le f(\beta) \tag{19}$$

where, $k = 1, 2, \cdots, n$.

If $f(a) \le f(\beta)$, it is a high-quality particle, otherwise it is a low-quality particle. If agent a is the high-quality particle, its position in the solution space will remain unchanged. On the contrary, agent a will update the position in the solution according the following formula:

$$a_k' = \beta_k + rand(-1,\ 1)(\beta_k - a_k) \tag{20}$$

where, rand (−1, 1) is random number within the interval of (−1, 1). If $a_k' > x_{k\max}$, then $a_k' = x_{k\max}$. $x_{k\min}$, $x_{k\max}$ is the lower and upper limit of the feasible solution space of the optimization problem.

(4) Agent particle updating in the solution space. The position and speed of each agent particle is updated in the solution space. According to PSO iteration formula [33]:

$$\begin{cases} v_{iD} = wv_{iD} + c_1r_1(p_{iD} - x_{iD}) + c_2r_2(p_{gD} - x_{iD}) \\ x_{iD} = x_{iD} + v_{iD} \end{cases} \tag{21}$$

where, set $c_1 = c_2 = 1.28$, $r_1 = r_2 = 0.54$.

(5) The fitness value calculation is based on CLS. Twenty percent of the particles with the best performance in the group is selected to conduct chaotic local search. The individual extreme value of each particle and all values in the group are updated. If the algorithm meets the end condition of optimization, the search stops and the optimal solution is obtained and parameters (K_{dcP}, K_{dcI}) are obtained. Otherwise, the algorithm turns to step (6).

(6) Fitness recalculation of each particle. The search region is shrunk according to the following formula [32]:

$$\begin{cases} x_{\min i} = \max(x_{\min i}, x_{gi} - r(x_{\max i} - x_{\min i})) \\ x_{\max i} = \min(x_{\max i}, x_{gi} + r(x_{\max i} - x_{\min i})) \end{cases} \tag{22}$$

where x_{gi} is the i dimension variable of the current individual extreme value. The remaining 80% of the particles in the population are generated in the contracted space, and the algorithm turns to step (2).

After that, I_{dR} is the output that is optimized by CPSO-MAS in the voltage PI controller. The I_{dR} with capacitance current I_{dc} generates a PWM signal which drivers IGBT to output the DC-link bus voltage u_{dc}.

5. UPQC Harmonic Detection and Control Strategy

In order to validate the effectiveness of the DC-link bus voltage control strategy, the harmonic elimination in the UPQC is taken as an example to illustrate the influence of the DC-link bus voltage control to the UPQC performance. The schematic of the harmonic detection based on $i_p - i_q$ in the PAPF of the UPQC is shown in Figure 9.

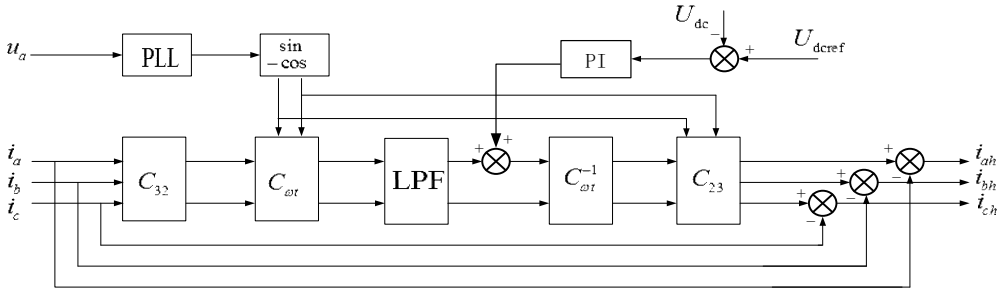

Figure 9. Harmonic detection schematic.

Where i_a, i_b, i_c is load current, u_a is the grid voltage of phase a which provides voltage phase signal via phase locked loop (PLL). i_α and i_β are calculated by C_{32} transformation according to i_a, i_b, i_c. i_p and i_q are obtained with $C_{\omega t}$ transformation according to i_α, i_β. Next, i_{pf} and i_{qf}, i.e., the fundamental positive sequence component of i_p and i_q, are gained through a low pass filter (LPF). Next, the three-phase fundamental current i_{af}, i_{bf} and i_{cf} are obtained by calculation of $C_{\omega t}^{-1}$ and C_{23}, respectively. Thereby, the compensation current signal instructions of UPQC, i.e., i_{ah}, i_{bh}, and i_{ch} are obtained according to Figure 10.

where

$$C_{32} = \sqrt{\frac{2}{3}}\begin{bmatrix} 1 & -\frac{1}{2} & -\frac{1}{2} \\ 0 & \frac{\sqrt{3}}{2} & -\frac{\sqrt{3}}{2} \end{bmatrix}, C_{\omega t} = \begin{bmatrix} \sin\omega t & -\cos\omega t \\ -\cos\omega t & -\sin\omega t \end{bmatrix}, C_{23} = \sqrt{\frac{2}{3}}\begin{bmatrix} 1 & 0 \\ -\frac{1}{2} & \frac{\sqrt{3}}{2} \\ -\frac{1}{2} & -\frac{\sqrt{3}}{2} \end{bmatrix}$$

Furthermore, in Figure 10, the DC-link bus voltage U_{dc} and reference voltage U_{dcref} forms a voltage loop by the PI controller in order to exchange energy between the PAPF and grid side when the PV charging module cannot provide enough energy. Then the obtained harmonic compensation instruction i_{ah}, i_{bh}, i_{ch} are obtained after subtraction between the instruction calculation current i_{af}, i_{bf}, i_{cf} and i_a, i_b, i_c. The PWM signals generated by harmonic compensation instruction drive the IGBT module to compensate the non-linear loads.

6. Analysis of Simulation

6.1. Simulation Model Establishment

According to the proposed PV charging control scheme for the DC-link bus of the UPQC, a simulation model was developed to verify the correctness and effectiveness of the proposed control strategy. Take an example of the UPQC harmonic compensation: the simulation model is a distribution network which includes a PV generation module, the PV DC-link charging module, PAPF module of the UPQC, and a non-linear load module. The non-linear load module is composed of a transformer and a rectifier, two groups of R-L load. The specific parameters are listed in Table 1.

To appropriately speed up the system simulation, the entire simulation system was discretized with the powerGUI module by using a discrete algorithm in Simulink. The sampling period was 1 μs.

Table 1. The parameters of the PAPF in the UPQC.

Parameters	Value
PV cell temperature	25 °C
Light intensity	1000 W/m^2
Cell numbers of PV1 module (for generating to grid)	100 pieces
Cell numbers of PV2 module (for DC-link Charging)	10 pieces
Cell power	250 W
PAPF DC-link side voltage	600 V
Capacity of DC-link side	100 μF/600 V
PAPF Filtering capacity C	1 μF/460 V
PAPF Filtering capacity R	100 Ω
PAPF Filtering capacity L	2 mH
Load (three-phase transformer)	380:380
Load (universal bridge)	0.001 Ω
Load1 (R, L)	7.5 Ω, 0.5 mH
Load2 (R, L)	5 Ω, 0.5 mH

6.2. Verification of UPQC DC-Link Bus Voltage Control Strategy

The UPQC was set to be connected to the distribution system at 0.05 s. Load2 was set to be parallel-connected to load1 at 0.1 s, and the total time of the simulation was 0.25 s. The verification of the UPQC DC-link bus voltage control strategy was conducted according to the voltage PI controller based on the standard PSO algorithm and CPSO-MAS algorithm. The DC-link bus voltage waveform is shown in Figure 10.

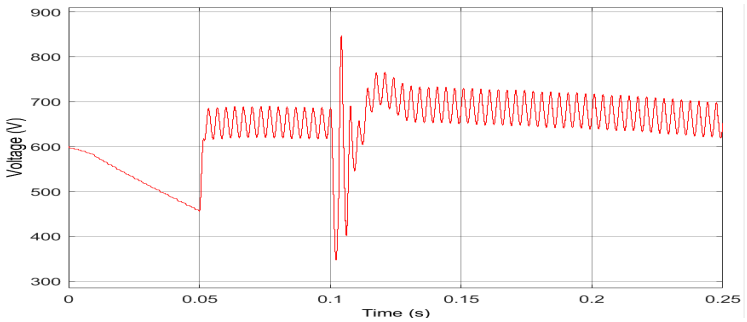

(**a**)

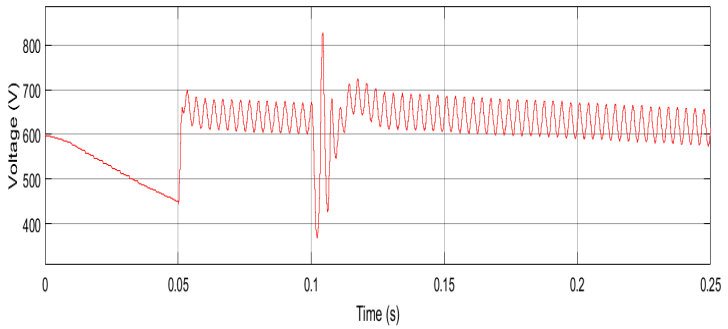

(**b**)

Figure 10. DC-link bus voltage waveform: (**a**) DC-link bus voltage waveform based on standard PSO algorithm. (**b**) DC-link bus voltage waveform based on CPSO-MAS algorithm.

From the DC-link bus voltage waveform based on different control algorithms, it was observed that the DC-link voltage of waveform of CPSO-MAS algorithm was toward 600 V faster than that of

the standard PSO algorithm. It was indicated that the CPSO-MAS algorithm had a faster convergence speed to the optimal parameter than the standard PSO algorithm.

6.3. Verification of UPQC Harmonic Compensation

In order to further verify the effect of the DC-link voltage control strategy on the improvement of power quality in a PV micro-grid, the harmonic compensation simulation was implemented, and the load current waveform in the micro-grid is shown in Figure 11.

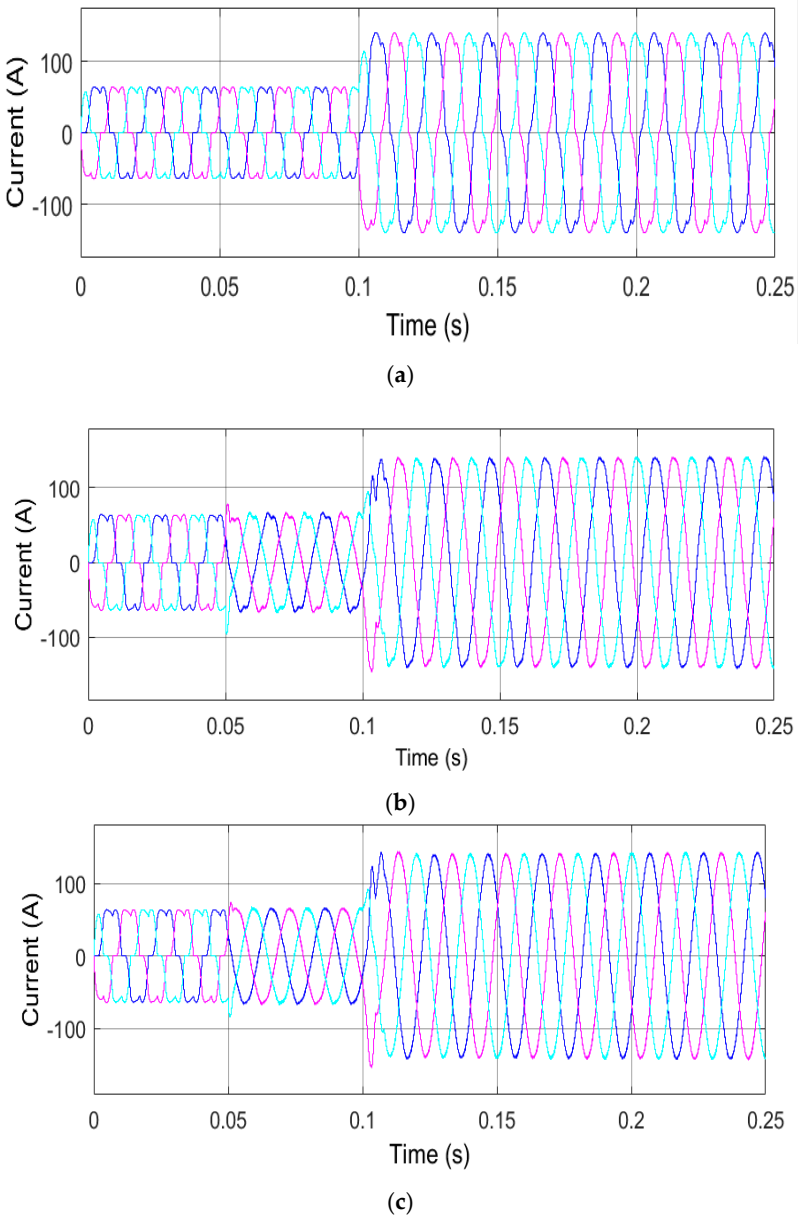

Figure 11. The current waveform of the grid side and load side. (**a**) Load current waveform uncompensated. (**b**) Grid current waveform compensated based on standard PSO algorithm. (**c**) Grid current waveform compensated based on CPSO-MAS algorithm.

From Figure 11a, it can be seen clearly that the waveform has a saw-toothed wave which indicates it contains harmonic components. Also, from Figure 11b,c, a saw-toothed wave appeared between 0 and 0.05 s. However, the harmonics were eliminated and the quality of the grid current improved due to the UPQC compensation at 0.05 s. Furthermore, it seems that the current waveform based on the

CPSO-MAS algorithm was smoother and more sinusoidal than that of the standard PSO algorithm. In addition, the current waveform was analyzed by FFT (Fast fourier transform) spectrum at t = 0.12 s, as is shown in Figure 12.

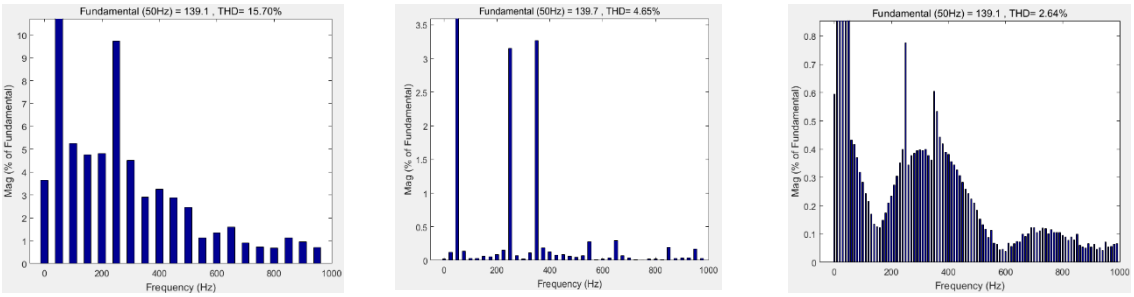

(**a**) (**b**) (**c**)

Figure 12. The utility grid current waveform spectrum. (**a**) Load current waveform spectrum uncompensated. (**b**) Grid current waveform spectrum compensated based on standard PSO algorithm. (**c**) Grid current waveform spectrum compensated based on CPSO-MAS algorithm.

From the current waveform spectrum, it can be clearly seen that total harmonic distortion (THD) value will be reduced from 4.65% to 2.64% if the PI controller optimized algorithm is changed from PSO to CPSO-MAS. Thereby, the comparison results prove that the algorithm of CPSO-MAS intensifies the optimization ability in total solution space due to the chaotic local search algorithm having the properties of randomness, ergodicity, and intrinsic regularity in the CPSO-MAS algorithm, and it overcomes the disadvantage that the PSO easily runs into part optimization.

7. Analysis of Experiments

7.1. The Micro-Grid Platform Establishment

In order to further validate the effectiveness of the DC-link bus voltage control strategy, the physical experiment on a laboratory prototype was developed. The hardware of the PAPF in the UPQC is presented in Figure 13. The main control chipset was DSP TMS320F27335. The hardware included a main control circuit, signal acquisition circuit, signal conditioning circuit, isolating circuit, IGBT drive circuit, filter circuit, etc.

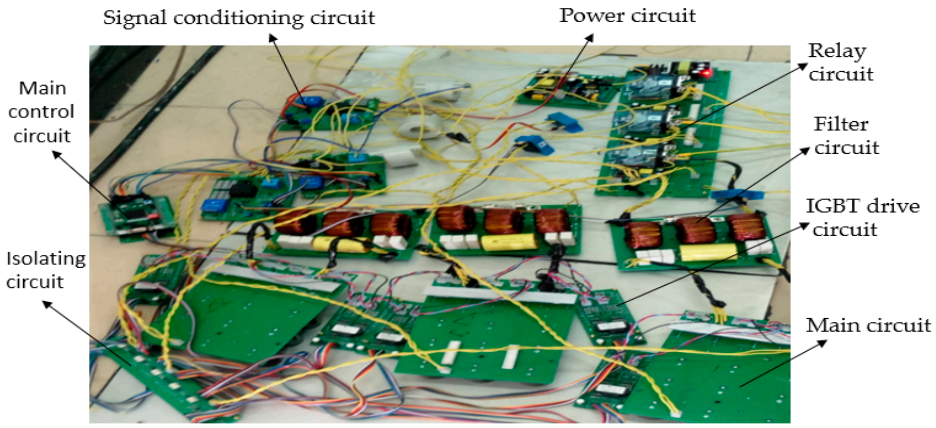

Figure 13. Hardware of the PAPF in the UPQC.

In Figure 13, the front of the main circuit in the PAPF is shown in Figure 14.

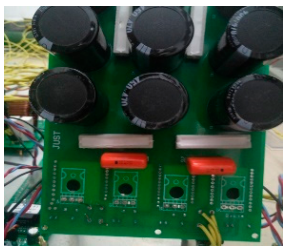

Figure 14. Front of the main circuit in the PAPF.

Then, the micro-grid platform was established in the lab as in Figure 15.

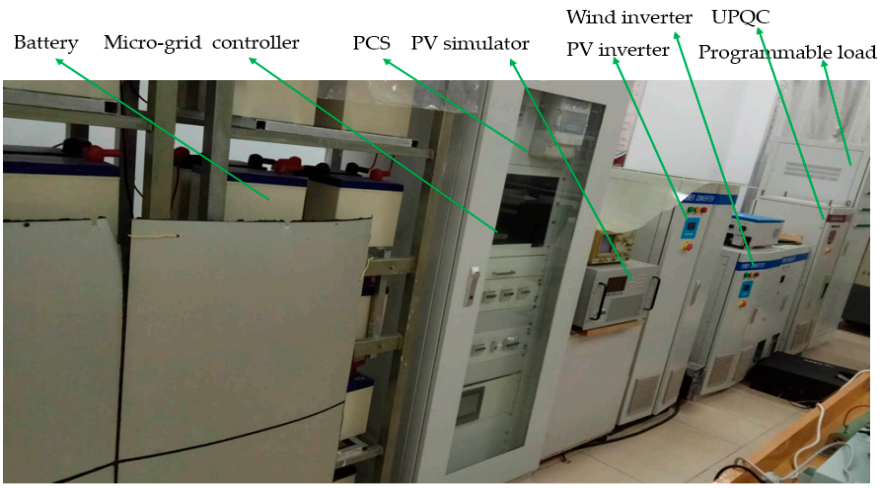

Figure 15. Micro-grid platform.

As is shown in Figure 15, the micro-grid platform included a battery, micro-grid controller, PCS (power conversion system), PV simulator and inverter, wind inverter and motor, programmable load, and prototype of the UPQC.

7.2. Experimental Results

Based on this platform, the experimental system configuration is elaborated in Table 2. According to the micro-grid type and load parameter, the experiment was divided into four cases to verify the feasibility of the proposed control algorithm. The micro-grid connected to the grid in parallel in the experiment and its three-phase three-wire system with three-phase voltage was 380 V. Take phase a as an example, the current was tested by current probe (Tektronix A622) and oscilloscope (TDS3034c), and the current probe scale selected was 100 mV/A.

Table 2. Experimental system configuration.

Case	Micro-Grid Type	Generation Parameter	Load Parameter
Case 1	PV micro-grid	PV 10 kW	P = 1100 W, Q_L = 1100 var Q_C = 200 var
Case 2	PV micro-grid	PV 10 kW	P = 100 W, Q_L = 1100 var,
Case 3	Hybrid micro-grid (PV, Wind, PCS)	PV 10 kW, Wind 5 kW, PCS 5 kW	P = 100 W, Q_L = 1100 var,
Case 4	Grid without micro-grid		P = 100 W, Q_L = 1100 var,

Case 1. The PV inverter was interfaced to the micro-grid in parallel, and the load is shown in Table 1, P = 1100 W, Q_L = 1100 var, and Q_C = 200 var. The load side current waveform is shown in Figure 16a, and the point of common coupling (PCC) side current waveform compensated by CPSO-MAS control strategy is shown in Figure 16b.

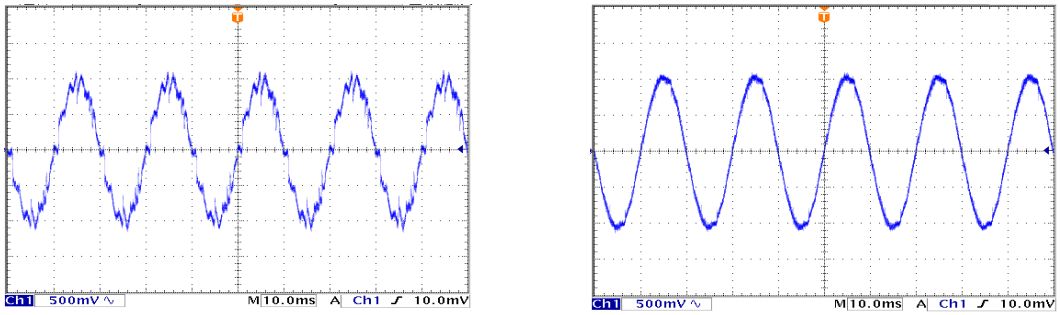

(**a**) (**b**)

Figure 16. Current waveform in the PV micro-grid. (**a**) Load side current waveform. (**b**) PCC side current compensated waveform.

Case 2. In this case, the load parameters were changed, P = 1100 W, Q_L = 1100 var. The load side current waveform is shown in Figure 17a, and the point of common coupling (PCC) side current waveform compensated by the proposed control strategy is shown in Figure 17b.

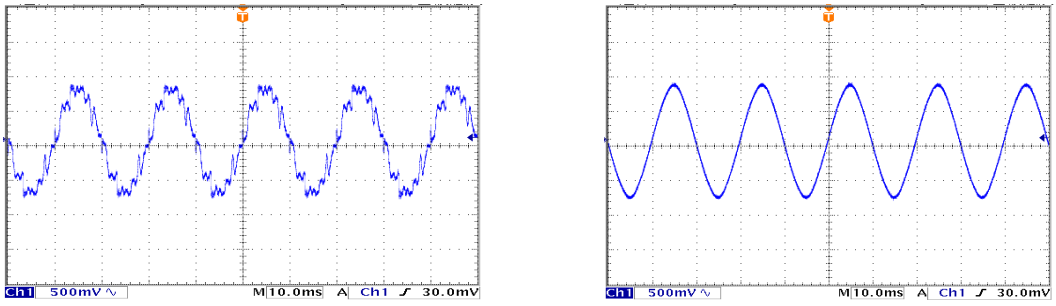

(**a**) (**b**)

Figure 17. Current waveform in the PV micro-grid. (**a**) Load side current waveform. (**b**) PCC side current compensated waveform.

Case 3. In this case, PV, PCS, and wind inverter are all connected to the micro-grid, and load parameters were with the same settings as Case 2. The load side current waveform is shown in Figure 18a, and the PCC side current waveform compensated by the proposed control strategy is shown in Figure 18b.

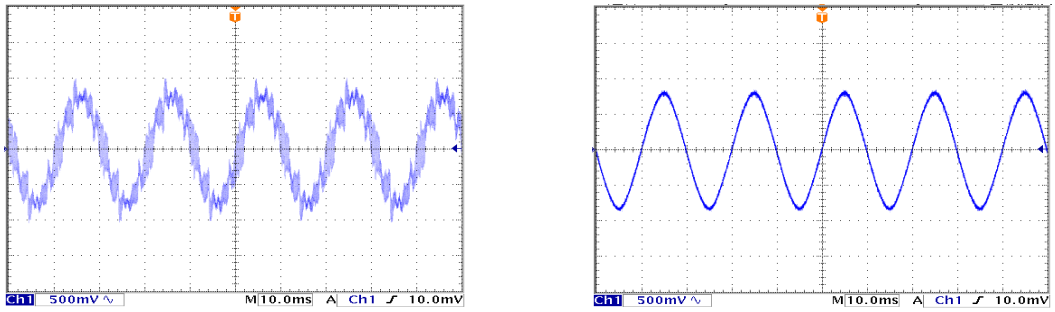

(**a**) (**b**)

Figure 18. Current waveform in the hybrid micro-grid. (**a**) Load side current waveform. (**b**) PCC side current compensated waveform.

Case 4. In this case, no distributed generation units were involved and load parameters had the same settings as Case 2. The load side current waveform is shown in Figure 19a and the PCC side current waveform compensated by the proposed control strategy is shown in Figure 19b.

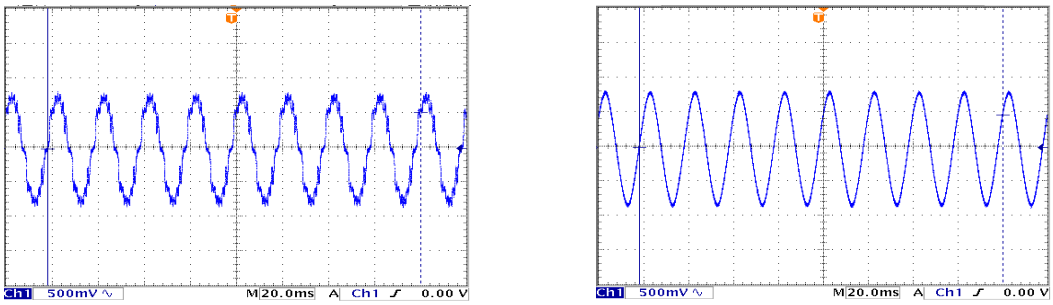

(**a**) (**b**)

Figure 19. Current waveform in the grid without the micro-grid. (**a**) Load side current waveform. (**b**) PCC side current compensated waveform.

Beside the current waveforms tested, the three-phase current spectrum were all tested by power quality analyzer (Fluke 430) in the experiment.

In Case 1, the load side current spectrum is shown in Figure 20a, and the PCC side current spectrum compensated by CPSO-MAS control strategy is shown in Figure 20b.

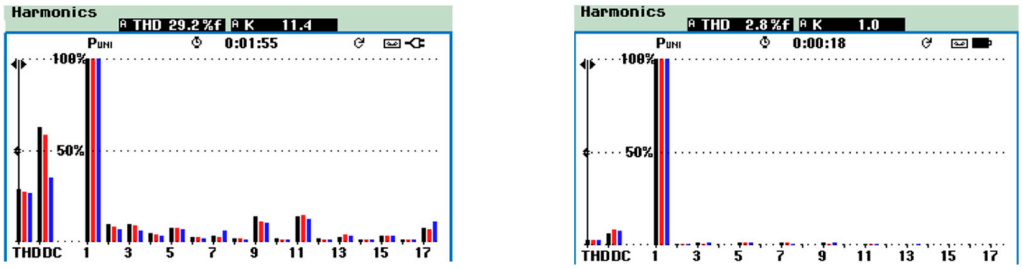

(**a**) (**b**)

Figure 20. Current spectrum in the PV micro-grid. (**a**) Load side current spectrum. (**b**) PCC side current compensated spectrum.

In case 2, the load side current spectrum is shown in Figure 21a, and the PCC side current spectrum compensated by the proposed control strategy is shown in Figure 21b.

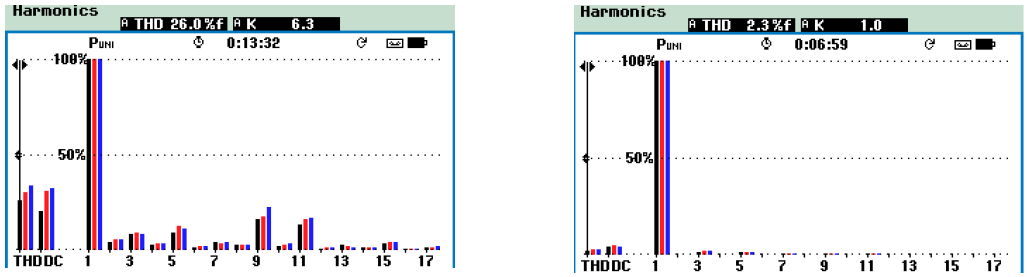

(**a**) (**b**)

Figure 21. Current spectrum in the PV micro-grid. (**a**) Load side current spectrum. (**b**) PCC side current compensated spectrum.

In Case 3, the load side current spectrum is shown in Figure 22a, and the PCC side current spectrum compensated by the proposed control strategy is shown in Figure 22b.

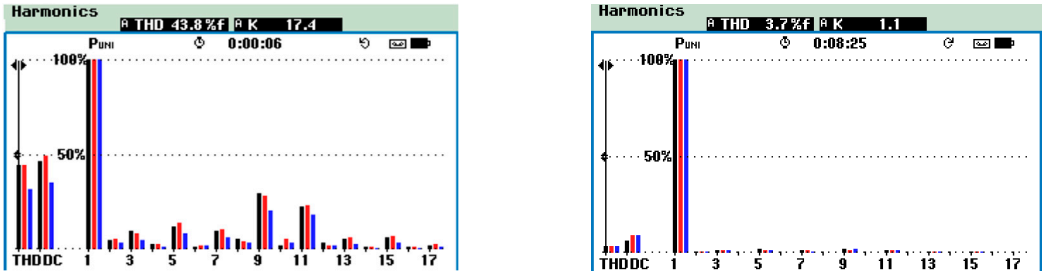

(**a**) (**b**)

Figure 22. Current spectrum in the PV hybrid micro-grid. (**a**) Load side current spectrum. (**b**) PCC side current compensated spectrum.

In Case 4, the load side current spectrum is shown in Figure 23a, and the PCC side current spectrum compensated by the proposed control strategy is shown in Figure 23b.

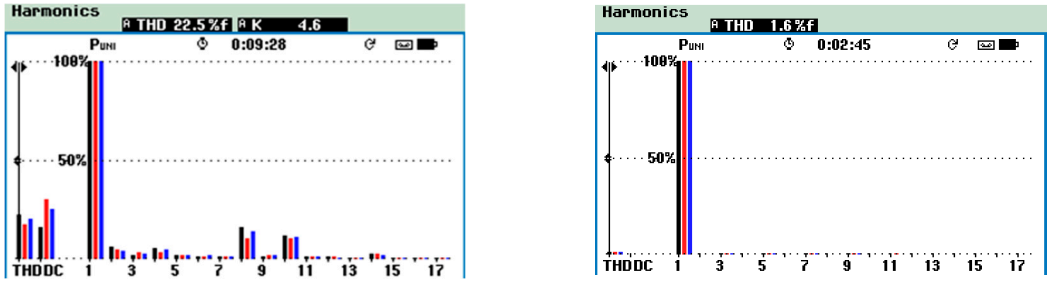

(**a**) (**b**)

Figure 23. Current spectrum in the grid without the micro-grid. (**a**) Load side current spectrum. (**b**) PCC side current compensated spectrum.

7.3. Discussion

According to Figures 18a and 19a, it can be seen that power quality of the distributed network gets worse with the penetration of distributed generation units, with clear burrs and saw-toothed waveforms, particularly for the case of the containing hybrid micro-grid. This also can be illustrated by Figure 22a, where Case 3 gave the worst THD value, 43.8% without compensation, and Case 4 (grid without micro-grid) showed lower THD value, 22.5% than that in the same load. Regarding different load settings, the case with more non-linear load derives higher THD, with the value of 26.0% (Case 2) versus 29.2% (Case 1), indicating worse power quality. By applying UPQC, the power quality was significantly improved as displayed in Figures 20–23, for all four cases, with the THD decreased clearly, the power quality was improved well by the UPQC. Hence, it can be concluded that CPSO-MAS algorithm was fairly effective in harmonic compensation of the UPQC.

8. Conclusions

A CPSO-MAS-based control scheme of the DC-link bus integrated PV charging module in the UPQC was proposed in this paper. The strategy is capable of improving the power quality in the micro-grid. Through the simulation and experiment of the UPQC harmonic compensation, the compensated current waveform based on the CPSO-MAS algorithm was smooth and nearly

sinusoidal. The THD value of the spectrum of the current compensated waveform meets the national standard of power quality. In addition, it was validated that the proposed DC-link bus voltage control strategy had faster convergence than other algorithms, which enhances the stability of the DC-link bus voltage. All in all, the proposed control strategy demonstrated to be effective in applying the UPQC towards various conditions related to voltage and current distortion.

Author Contributions: F.N. created UPQC models, developed methodology, wrote the initial draftand designed the hardware, Z.L. supervised and leaded responsibility for the research activity planning, and Q.W. designed the hardware, reviewed and edited the paper. Authorship must be limited to those who have contributed substantially to the work reported.

Funding: This work was supported in part by the National Natural Science Foundation of China (51477070); in part by National Key R&D Program of China (017YFB0103200); in part by Natural Science Foundation of the Higher Education Institutions of Jiangsu Province (17KJB470003).

Conflicts of Interest: The authors declare no conflict of interest.

References

1. Khadem, S.K.; Basu, M.; Conlon, M.F. Intelligent Islanding and Seamless Reconnection Technique for Microgrid with UPQC. *IEEE J. Emerg. Sel. Top. Power Electron.* **2015**, *3*, 483–492. [CrossRef]
2. Magdy, G.; Mohamed, E.A.; Shabib, G.; Elbaset, A.A.; Mitani, Y. Microgrid dynamic security considering high penetration of renewable energy. *Prot. Control Mod. Power Syst.* **2018**, *3*, 236–246. [CrossRef]
3. Sachin, D.; Bhim, S. Design and Performance Analysis of Three-Phase Solar PV Integrated UPQC. *Ind. Appl.* **2018**, *54*, 73–81.
4. Sachin, D.; Bhim, S. Modified pq-Theory-Based Control of Solar-PV-Integrated UPQC. *Ind. Appl.* **2017**, *53*, 5031–5040.
5. Shubh, L.; Sanjib, G. Modelling and allocation of open-UPQC integrated PV generation system to improve the energy efficiency and power quality of radial distribution networks. *IET Renew. Power Gener.* **2018**, *12*, 605–613.
6. Sanjib, G. Multi-Objective Planning for Reactive Power Compensation of Radial Distribution Networks with Unified Power Quality Conditioner Allocation Using Particle Swarm Optimization. *Power Syst.* **2014**, *29*, 1801–1810.
7. Vinod, K. Enhancing electric power quality using UPQC: A comprehensive overview. *IEEE Trans. Power Electron.* **2012**, *27*, 2284–2297.
8. Vinod, K. Fixed and variable power angle control methods for unified power quality conditioner: Operation, control and impact assessment on shunt and series inverter kVA loadings. *IET Power Electron.* **2013**, *6*, 1299–1307.
9. Sanjib, G. Unified power quality conditioner allocation for reactive power compensation of radial distribution networks. *IET Gener. Transm. Distrib.* **2014**, *8*, 1418–1429.
10. Bharath, B.A.; Vinod, K. Optimal Sizing of UPQC Considering VA Loading and Maximum Utilization of Power-Electronic Converters. *Power Deliv.* **2014**, *29*, 1490–1498.
11. Xu, Q.M.; Ma, F.J.; Luo, A.; He, Z.X. Analysis and Control of M3C-Based UPQC for Power Quality Improvement in Medium/High-Voltage Power Grid. *Power Electron.* **2016**, *31*, 8182–8194. [CrossRef]
12. Abdul, M.R.; Amit, V.S.; Vinod, K. A Novel Ten-Switch Topology for Unified Power Quality Conditioner. *Power Electron.* **2016**, *31*, 6937–6946.
13. Srinivas, B.; Karanki, N.G. A Modified Three-Phase Four-Wire UPQC Topology with Reduced DC-Link Voltage Rating. *Ind. Electron.* **2013**, *60*, 3555–3566.
14. Cheung, V.S.; Yeung, R.S.; Henry, S.H.; Alan, W.L. A Transformer- Less Unified Power Quality Conditioner with Fast Dynamic Control. *Power Electron.* **2018**, *33*, 3926–3937. [CrossRef]
15. Kian, H.K.; Ping, L.S.; Chu, Y.C. An Output Regulation-Based Unified Power Quality Conditioner with Kalman Filters. *Ind. Electron.* **2012**, *59*, 4248–4262. [CrossRef]
16. Ni, F.; Li, Z.; Wang, Q.; Wo, S. UPQC Voltage Sag Detection Based on Chaotic Immune Genetic Algorithm. *Clust. Comput.* **2016**, *19*, 1–13.
17. Ahmet, T.; Mehmet, E.M.; Mehmet, U.C.; Mehmet, T.; KamilÇ, B. Open unified power quality conditioner with control based on enhanced phase locked loop. *IET Gener. Transm. Distrib.* **2013**, *7*, 254–264.

18. Hossein, H.; Gabriele, D.; Alessio, D.; Davide, D.G.; Roberto, F.; Giovanni, M. Power Quality Conditioning in LV Distribution Networks: Results by Field Demonstration. *Smart Grid* **2017**, *8*, 418–427.
19. Feng, X.T.; Ma, W.Z.; Huo, Q.H. Coordinated control strategy based on reactive power flow in UPQC. *Electr. Mach. Control* **2013**, *17*, 1–5.
20. Rajesh, K.P.; Kamalakanta, M. High-performance unified power quality conditioner using non-linear sliding mode and new switching dynamics control strategy. *IET Power Electron.* **2017**, *10*, 863–874.
21. Ye, J.; Gooi, H.B. Optimization of the Size of UPQC System Based on Data-Driven Control Design. *Smart Grid* **2018**, *9*, 2999–3008. [CrossRef]
22. Ye, J.; Gooi, H.B.; Wu, F.J. Optimal Design and Control Implementation of UPQC Based on Variable Phase Angle Control Method. *Ind. Inform.* **2018**, *14*, 3109–3123. [CrossRef]
23. Rajesh, K.P.; Kamalakanta, M. High-performance unified power Quality conditioner using command generator tracker-based direct adaptive control strategy. *IET Power Electron.* **2016**, *9*, 1267–1278.
24. QuocNam, T.; Lee, H.H. Improvement of unified power quality conditioner performance with enhanced resonant control strategy. *IET Gener. Transm. Distrib.* **2014**, *8*, 2114–2123.
25. Jia, D.Q.; Wei, T.Z.; Huo, Q.H. Small Signal Analysis and Coordinated Control Strategy of UPQC Switching. *Autom. Electr. Power Syst.* **2014**, *38*, 187–195.
26. Tan, Z.; Zhu, D.; Chen, J. DC Side Capacitor Voltage Fluctuation Reason and Inhibition Method for Three-phase Four-wire UPQC. *Autom. Electr. Power Syst.* **2010**, *34*, 61–65.
27. Li, C.; Rong, Y.; Cao, L.; Zheng, X.S. Adaptive Control for Single-Phase Unified Power Quality Conditioner Using Neural Networks. In Proceedings of the Second International Conference on Bio-Inspired Computing: Theories and Applications, Zhengzhou, China, 14–17 September 2007; pp. 146–150.
28. Yang, D.L.; Lu, Z.G.; Hang, N.S. Unified power quality conditioner using emotional intelligent controller. *Power Syst. Prot. Control* **2013**, *41*, 118–124.
29. Axente, I.; Basu, M.; Conlon, M.F. DC link voltage control of UPQC for better dynamic performance. *Electr. Power Syst. Res.* **2011**, *81*, 1815–1824. [CrossRef]
30. Raphael, J.; Millnitz, D.S.; Jean, C.C.; Marcello, M. A Simplified Control Technique for a Dual Unified Power Quality Conditioner. *Ind. Electron.* **2014**, *61*, 5851–5860.
31. Ni, F.Y.; Li, Z.M.; Shen, L. The PV MPPT Control Strategy Based on Generalized Predictive Control. *Open Fuels Energy Sci. J.* **2015**, *8*, 244–251.
32. Liu, L.M.; Kang, Y.; Chen, J.; Zhu, P.C. Static Synchronous Series Compensator: Modeling. *Control Scheme Perform.* **2006**, *21*, 37–43.
33. Tang, X.L.; Zhang, H.; Zhou, J.L.; Zhang, Y. PID Controller of Magnetic Suspension System Based on CPSO in Multi-agent Architecture. *Inf. Control* **2013**, *42*, 758–764.
34. Zhao, B.; Cao, Y.J. A multi-agent Particle Swarm Optimization Algorithm for Reactive Power Optimization. *Proc. CSEE* **2005**, *25*, 1–7.
35. Tang, X.L.; Li, Y.; Li, P.; Liu, N.C. Model predictive control based on SVR Optimized by multi-agent particle swarm optimization algorithm. *Control Decis.* **2014**, *29*, 593–598.
36. Tang, X.L.; Cheng, X.; Wang, B.Q. Distribution Network Reconfiguration Adopting Chaos Particle Swarm Algorithm of Multi-Agent System. *Proc. CSU-EPSA* **2015**, *27*, 17–23.
37. Zhao, S.Y.; Liu, W.; Cai, Y.H. Artificial Bee Colony Algorithm Based on Improvement of Chaotic Local Search. *J. Guangdong Univ. Technol.* **2013**, *30*, 55–60.